Local density of states fluctuations in a two-dimensional superconductor as a probe of quantum diffusion

Mathieu Lizée, Matthias Stosiek, Igor Burmistrov, Tristan Cren, Christophe Brun

Editors' Suggestion

Local density of states fluctuations in a two-dimensional superconductor as a probe of quantum diffusion

Mathieu Lizée,[1,2,*] Matthias Stosiek,[3] Igor Burmistrov,[4,5,†] Tristan Cren,[2] and Christophe Brun[2,‡]

[1]*Laboratoire de Physique de l'École Normale Supérieure, ENS, Université PSL, CNRS, 3 Sorbonne Université, Université Paris Cité, 75005 Paris, France*

[2]*Sorbonne Universite, CNRS, Institut des Nanosciences de Paris, UMR7588, 75252 Paris, France*

[3]*Physics Division, Sophia University, Chiyoda-ku, Tokyo 102-8554, Japan*

[4]*L. D. Landau Institute for Theoretical Physics, Akademika Semenova Avenue 1-a, 142432 Chernogolovka, Russia*

[5]*Laboratory for Condensed Matter Physics, HSE University, 101000 Moscow, Russia*

(Received 27 January 2023; accepted 7 April 2023; published 8 May 2023)

The interplay of superconductivity and disorder generates a wealth of complex phenomena. In particular, the peculiar structure of diffusive electronic wave functions is predicted to increase the superconducting critical temperature in some range of disorder. In this work, we use an epitaxial monolayer of lead showing a simple band structure and homogeneous structural disorder as a model system of a two-dimensional superconductor in the weak-antilocalization regime. Then, we perform an extensive study of the emergent fluctuations of the local density of states (LDOS) and spectral energy gap in this material and compare them with both analytical results and the numerical solution of the attractive Hubbard model. We show that mesoscopic LDOS fluctuations allow us to probe locally both the elastic and inelastic scattering rates, which are notoriously difficult to measure in transport measurements.

DOI: 10.1103/PhysRevB.107.174508

I. INTRODUCTION

Since the seminal paper by Anderson, the field of wave localization in disordered media has developed immensely. In the metallic regime, mesoscopic fluctuations of conductance stemming from the diffusion of electrons in a quenched disorder potential have been observed in a wealth of condensed-matter systems and are commonly referred to as the "weak-localization" signature [1]. A similar signature of weak localization is predicted to emerge in maps of the local density of states (LDOS) of two-dimensional (2D) metallic systems [2–4] and has already been observed for surface-plasmon modes [5,6]. For electronic modes, however, despite several reports of electronic LDOS spatial fluctuations [7–10], theoretical predictions still lack a quantitative comparison with experiments.

The interplay of disorder and superconductivity has recently received renewed experimental (see Refs. [11,12] for a review) and theoretical interest [13–24]. In particular, the pairing of weakly localized "multifractal" electrons was surprisingly predicted to yield a disorder-enhanced T_c compared to the clean metal case in well-chosen conditions [25,26]. Recently, an experimental demonstration of a possible multifractal enhancement of T_c in $NbSe_2$ monolayers was reported [9]. Subsequently, the spatial distribution of the superconducting gap in this material recently demonstrated multifractal statistics [27]. However, a clear picture of multifractal superconductivity is still lacking because the multifractal properties of the underlying eigenstates were not revealed in systematic LDOS measurements. In addition, a recent study suggested clearly that this experimental material presents the inverse proximity effect from the graphene bilayer, making it more of an superconductor-normal metal bilayer than a pure 2D single layer [28]. Thus, a deeper understanding of 2D diffusive superconductors in the multifractal regime is now required to strengthen this discovery and stimulate the engineering of multifractally enhanced superconductors.

In this study, we probe the mesoscopic fluctuations of the LDOS in a purely two-dimensional weakly disordered superconductor with high-resolution scanning tunneling spectroscopy (STS). In contrast to previous STS studies on thin films [29–34] and $NbSe_2$ monolayers [9,27], we prove quantitatively that coherent electronic diffusion controls both the LDOS fluctuations close to the superconducting coherence peaks and the spectral energy gap fluctuations. To generalize our interpretation, we compare our measurements with self-consistent solutions of the attractive Hubbard model on a state-of-the-art system size [19,22]. We demonstrate that the energy dependence of mesoscopic LDOS fluctuations allows us to extract both the elastic and inelastic scattering rates of low-energy single-particle excitations and argue that LDOS spatial fluctuations constitute a valuable toolbox for the study of 2D diffusive systems.

II. EXPERIMENTS

As model systems for the study of 2D weakly disordered electronic systems, epitaxial monolayers of metals on semiconducting surfaces are exceptionally interesting. First, their

*mathieu.lizee@phys.ens.fr
†burmi@itp.ac.ru
‡Corresponding author: christophe.brun@sorbonne-universite.fr

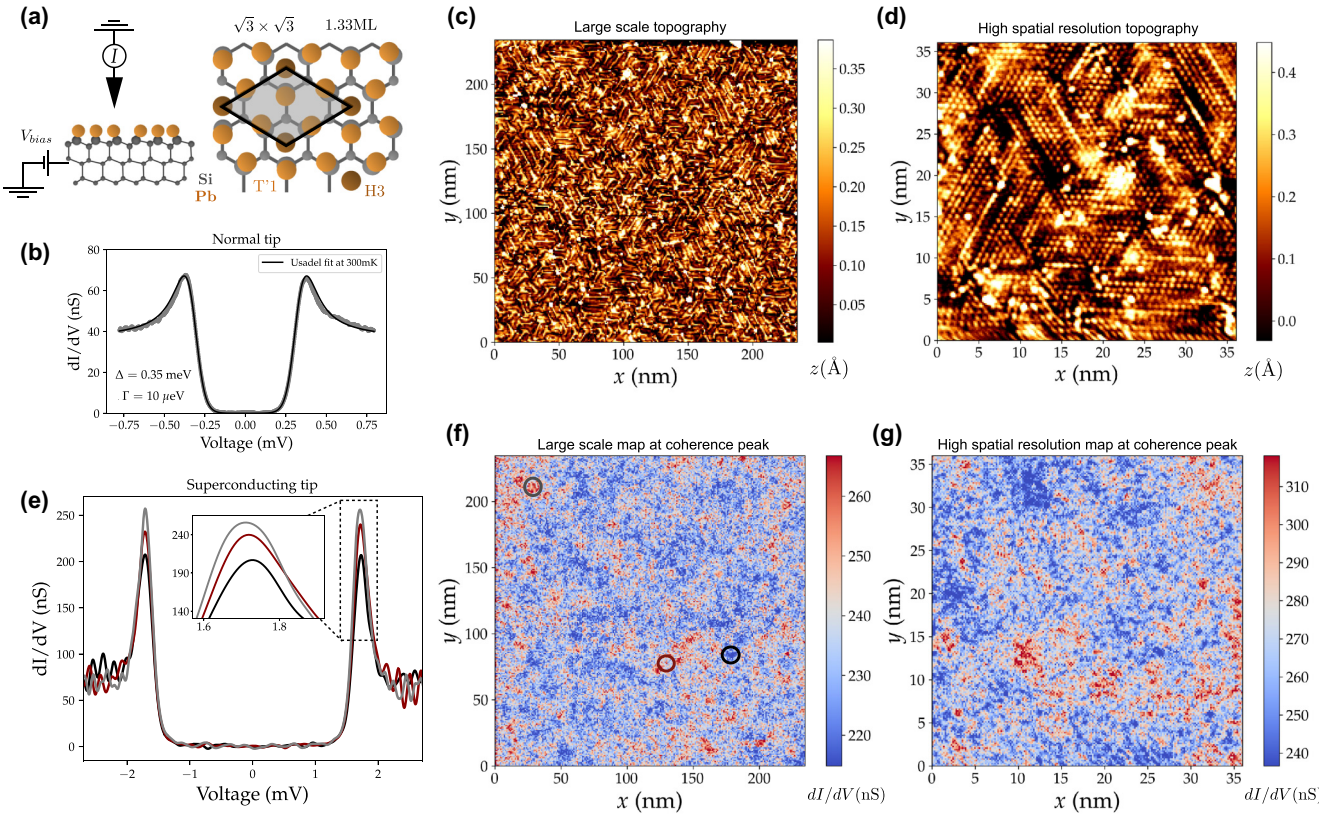

FIG. 1. Tunneling conductance fluctuations in the stripped incommensurate (SIC) phase of Pb/Si(111). (a) Description of the scanning tunneling spectroscopy measurement and of the SIC phase (1.33 ML of Pb/Si with $\sqrt{3} \times \sqrt{3}$ symmetry). (b) The tunneling conductance of the SIC phase measured with a platinum tip along with the best fit with the Usadel formula (see Appendix A). We find $\Delta_{\mathrm{SIC}} = 0.35$ meV and $\Gamma_{\mathrm{SIC}} = 10$ μeV. (c) Topographic image of the SIC monolayer phase. We clearly see the rotational nanodomains of the $\sqrt{3} \times \sqrt{3}$ phase separated by domain walls made of the $\sqrt{7} \times \sqrt{3}$ reconstruction. (d) An atomically resolved image. (e) Several differential conductance spectra (dI/dV) measured at the positions shown in (f). (f) The isoenergy map corresponding to topography in (c) at the coherence peak energy $V_{\mathrm{max}} = 1.7$meV. (g) Symmetrically, we show the isoenergy dI/dV map corresponding to the topography in (d) at the same bias voltage.

thickness, which is of the order of the Fermi wavelength, along with their good decoupling from the bulk makes them truly two-dimensional. Second, they show a wealth of phases with highly uniform and reproducible structural disorder without the need to evaporate chemical contaminants on the sample. Thus, these systems fully fabricated in ultrahigh vacuum are exceptionally clean and homogeneously disordered, in contrast to the usually studied substitution alloys [7–9], in which the disorder itself already has long-range correlations, as shown in the topographic maps in Refs. [8,9].

In this work, we focus on the stripped incommensurate (SIC) phase of lead on silicon. The ideal SIC monolayer described in Fig. 1(a) is made of 1.33 monolayers of lead atoms on top of a Si(111) surface. The lead is evaporated on the 7×7 reconstruction of silicon in a homemade scanning tunneling microscope. The SIC phase is made of nanometric domains oriented preferentially along three directions, as shown on a large scale in Figs. 1(c) and 1(d). The SIC phase has a nanometric mean free path much smaller than the superconducting coherence length $\xi \sim 50$ nm [35], making it a prototype system to study 2D diffusive superconductivity at weak disorder.

The sample is then cooled to 300 mK, well below its critical temperature of 1.8 K [36]. In Fig. 1(b), we show the tunneling spectroscopy at 300 mK measured with a platinum tip. The solid line is a solution of the Usadel equation for diffusive superconductors [37] (see Appendix A). The spectrum of Fig. 1(b) was fitted using a gap of $\Delta_{\mathrm{SIC}} = 0.35$ meV and a depairing energy of $\Gamma_{\mathrm{SIC}} = 10$ μeV. In order to probe the mesoscopic fluctuations of this phase, we acquired several large-scale (250×250 nm^2) spectroscopic maps with nanometric spatial resolution. A superconducting tip (bulk lead) is used to increase the energy resolution to 30 μeV [35,38]. The dI/dV spectrum [Fig. 1(e)] shows sharp coherence peaks at $V_{\mathrm{max}} \sim \Delta_{\mathrm{tip}} + \Delta_{\mathrm{SIC}} = 1.7$ mV. Three individual spectra whose positions are shown in Fig. 1(f) are displayed in Fig. 1(e).

Displaying the local differential conductance at a given bias voltage V_{bias} yields isoenergy dI/dV maps. In Figs. 1(f) and 1(g), we show the dI/dV map measured at the energy of the coherence peak (1.7 mV) and spatial fluctuations of the differential conductance spanning various scales below the superconducting coherence length $\xi \sim 50$ nm [35,38]. An interesting feature of this map is, indeed, that no characteristic scale can be easily identified. This fractal-like behavior is reminiscent of criticality close to the Anderson transition, driven by the cooperation of disorder and electronic coherence. The granular structure observed in the topography [see Figs. 1(c) and 1(d)] does not correlate at all with these "emergent"

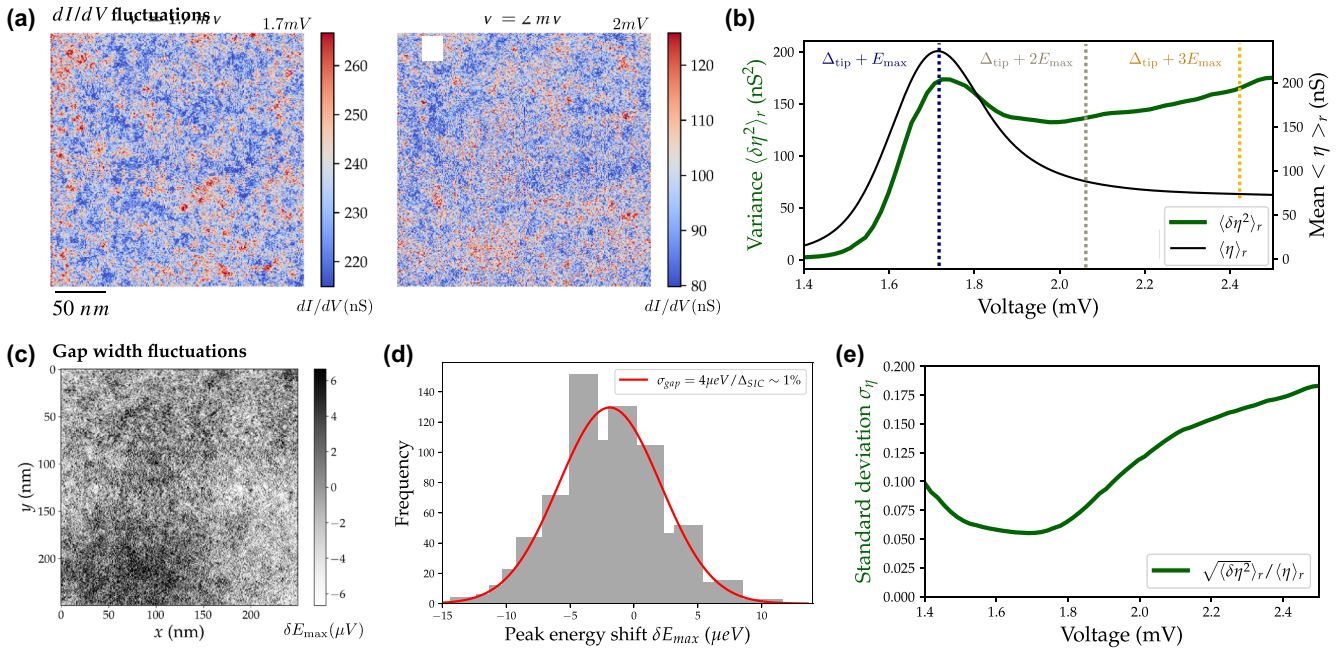

FIG. 2. Analysis of tunneling conductance fluctuations. (a) Isoenergy maps of the differential conductance $\eta = dI/dV$. (b) Variance (green) and mean value (black) of the tunneling conductance computed on isoenergy maps as a function of the bias voltage. (c) Map of the coherence peak energy fluctuations, corresponding to gap width fluctuations. (d) The distribution of this map, given along with a Gaussian distribution of standard deviation $\Sigma_{\text{gap}} = 4$ μeV. (e) The bias voltage dependence of the normalized standard deviation of dI/dV: $\sigma_{\text{exp}} = \sqrt{\langle \delta\eta(V)^2\rangle}/\langle\eta(V)\rangle$.

fluctuations, which we consequently attribute to coherent diffusion.

III. ANALYSIS OF FLUCTUATIONS

In order to reveal the superconducting properties in more detail, we focus on the LDOS spatial variance close to the superconducting coherence peaks. At voltage V, the variance of isoenergy tunneling conductance maps [shown in Fig. 2(a) for $V \in \{1.7, 2\}$ mV] is written as $\sigma^2_{\text{exp}}(V) = \langle \delta(\frac{dI}{dV})^2\rangle_r$, where to keep notations brief, $\eta = dI/dV$ is the experimentally measured differential conductance (see Sec. III D for a more accurate definition) and the brackets denote spatial averaging. In Fig. 2(b), we plot (in green) the variance $\langle \delta\eta^2\rangle$ as a function of bias voltage, showing a maximum close to the coherence peak energy $V_{\text{max}} = E_{\text{max}} + \Delta_{\text{tip}} = 1.7$ mV. The normalized standard deviation is plotted in Fig. 2(e) and shows a characteristic minimum close to E_{max} followed by a convex increase at higher energy. As shown in Appendix E, the normalized standard deviation of the LDOS is symmetric with respect to the Fermi level (i.e., negative and positive bias voltages). As gap width granularity is a standard feature of 2D superconductors [9,12,27,39], we plot the fluctuations of the peak energy E_{max} in Fig. 2(c). The distribution [see Figs. 2(d)] shows a relative standard deviation $\sigma_{E_{\text{max}}}$ of about 1%, much smaller than the relative fluctuations of the LDOS shown in Fig. 2(e) ranging from 6% to 20%.

A. Semianalytical theoretical predictions

To rationalize the energy dependence of the LDOS spatial variance, we now compute the fluctuations of the density of states $\rho(E, \boldsymbol{r})$ in a 2D diffusive superconductor. In the following, we sketch a simplified derivation. Like in the mean-field solution to the BCS Hamiltonian, we introduce the Bogoliubov operators and coherence factors $u^2_\alpha/v^2_\alpha = (1 \pm \epsilon_\alpha/\sqrt{\epsilon_a^2 + \Delta^2})/2$ associated with the single-particle eigenstates ϕ_α for the eigenvalue ϵ_α, which are the solutions of the single-particle Schrödinger equation including the disordered potential. The LDOS can be written conveniently as

$$\rho(E, \boldsymbol{r}) = \sum_{\alpha, s=\pm} \phi^2_\alpha(\boldsymbol{r})(1 + \epsilon_\alpha/E)\delta\big(E - s\sqrt{\epsilon^2_\alpha + \Delta^2}\big). \quad (1)$$

Here, $s = \pm$ denotes states above and below the Fermi level, respectively. The density of states correlations are then computed from this expression along with the dynamical structure factor, which is a spatially averaged product of wave functions measured at positions $\boldsymbol{r}$ and $\boldsymbol{r}'$ and at well-determined energies. If one neglects the dependence of the single-particle density of states on energy in the normal state, this structure factor can be computed from the polarization operator $\Pi^R(\omega, \boldsymbol{r}, \boldsymbol{r}')$ (see, e.g. [40]),

$$F(\epsilon, \omega, \boldsymbol{r}, \boldsymbol{r}') \simeq \frac{1}{\pi\omega}\text{Im}\,\Pi^{\text{R}}(\omega, \boldsymbol{r}, \boldsymbol{r}'). \quad (2)$$

In the *diffusive regime at weak disorder*, one gets, for the Fourier transform of the polarization operator,

$$\Pi^R(\omega, \boldsymbol{q}) = \rho_0 \frac{Dq^2}{Dq^2 - i\omega}, \quad (3)$$

where D denotes the diffusion coefficient and ρ_0 is the density of states of the noninteracting problem at the Fermi level. The full derivation then yields the pair LDOS correlation function

at different spatial points $(\boldsymbol{r_1}, \boldsymbol{r_2})$ and different energies (E_1, E_2) [21–23]:

$$\langle \delta\rho(E_1, \boldsymbol{r}_1)\delta\rho(E_2, \boldsymbol{r}_2)\rangle = \frac{\rho_0^2}{2\pi g}\mathrm{Re}\left\{[1 + X_{E_1}X^*_{E_2}]K_0\left(R\sqrt{\frac{2\gamma_\Phi - iE_1/X_{E_1} + iE_2/X^*_{E_2}}{\hbar D}}\right)\right.$$
$$\left. - [1 - X_{E_1}X_{E_2}]K_0\left(R\sqrt{\frac{2\gamma_\Phi - iE_1/X_{E_1} - iE_2/X_{E_2}}{\hbar D}}\right)\right\}, \tag{4}$$

where $R = |\boldsymbol{r}_1 - \boldsymbol{r}_2|$ and $K_0(z)$ stands for the modified Bessel function. Also, we introduce $X_E = E/\sqrt{E^2 - \Delta_E^2}$, where we phenomenologically substitute Δ with the complex energy-dependent gap function Δ_E, which we estimate using the Usadel model for diffusive superconductors (see Appendix A). We check that, as observed experimentally, Eq. (4) is symmetric with respect to the Fermi level: $E_1 = E_2 = V$ and $E_1 = E_2 = -V$ yield the same correlations. Finally, two parameters control the strength of LDOS fluctuations: the dimensionless conductivity $g = hD\rho_0/2$ and the effective dephasing rate $\gamma_\Phi = \hbar D/L_\Phi^2$, which we assume are energy independent. We note that strong spin-orbit coupling results in a factor of $1/4$ (in comparison with the case when spin-orbit coupling is absent) due to suppression of triplet diffusons. This well-known fact (see, e.g., Ref. [41]) was taken explicitly into account in Eq. (4) (see Ref. [23]). In Fig. 3(a), we show the energy dependence of the density of states normalized variance $\sigma_\rho^2(E) = \langle \delta\rho(E)^2\rangle_r/\langle\rho(E)\rangle_r^2$. Here, the conductance is fixed at $g = 30$, and we show the plots for several values of γ_Φ typically ranging between $\Gamma \sim k_BT \sim 30\,\mu$V and $\Delta \sim 350\,\mu$V. In black, we show the spectrum of the mean density of states where $\mathrm{Re}(X_E)$ used in this computation corresponds to the best Usadel fit for the SIC phase (see Appendix A). We show that σ_ρ^2 has a local minimum close to the coherence peak energy $E_{\max}$, in good agreement with the minimum of normalized variance $\sigma^2_{\exp}$ at the superconducting coherence peak [Fig. 2(c)]. In Figs. 3(b) and 3(c), we show that at fixed energy, σ_ρ^2 decreases with increasing conductivity [as expected from the $1/g$ dependence in Eq. (4)]. In Figs. 3(b) and 3(d), we demonstrate that increasing the dephasing rate γ_Φ, corresponding to a smaller system size in a transport experiment (Thouless energy), reduces the variance σ_ρ^2. We stress that these dependences are very natural in the context of mesoscopic fluctuations. A larger electronic phase coherence length and stronger disorder lead to enhanced fluctuations, whether one measures conductance in transport experiments or the LDOS with a scanning tunneling microscope.

B. Electronic diffusion in the SIC phase and quantitative extraction of transport parameters

In order to compare the amplitude of the LDOS fluctuations with theoretical predictions, we evaluate the diffusion coefficient in the SIC phase by independent means. We refer to previous work by some of the authors in which the proximity effect between the SIC phase and small bulky lead islands allowed them to estimate the diffusion coefficient of the monolayer [35]. These results are supported by another measurement in which the spatial profile of a vortex core allowed us to extract the effective coherence length in the diffusive limit and thus the electronic diffusion coefficient [38]. Both these measurements yield a dirty coherence length $\xi \in [45, 50]$ nm. Writing $\xi = \sqrt{\hbar D/\Delta_{\mathrm{SIC}}}$ with $\Delta_{\mathrm{SIC}} = 0.35$ meV gives a diffusion coefficient $D \in [10, 15]$ cm^2/s. We now consider the Einstein relation for the conductivity (per spin orientation) of the monolayer $g = hD\rho_0/2$, and using the 2D electron gas model (shown to be appropriate by angle-resolved photoemission spectroscopy measurements [42]), we write for the density of states $\rho_0 = 2\frac{k_F}{hv_F} = \frac{2m}{2\pi\hbar^2}$ (the factor of 2 is for the two spin orientations). This leaves us with $g = \frac{mD}{\hbar}$. Using the known effective mass $m = 1.27m_e$ in the SIC phase [36], we can estimate $g \sim 20$. We insist that this value may be underestimated because in the former experiments used to evaluate ξ, the disorder was higher than in the present experiment due to scattering nanoislands that do not appear here. Thus, we infer that $g = 20$ is, in fact, a lower bound of the actual conductance, and we roughly estimate $g \in [20 - 100]$. Like we stated earlier, the lead monolayer is weakly disordered and lies deep in the diffusive regime as the mean free path $\ell \sim 1$–5 nm is much smaller than ξ.

C. Gap width fluctuations

For a diffusive 2D superconductor in the weak-disorder regime, fluctuations of $E_{\max}$ can be estimated theoretically (see Appendix D). We find $\sigma_{E_{\max}} \simeq \sqrt{c/g}(\Gamma_{\mathrm{SIC}}/\Delta_{\mathrm{SIC}})^{2/3}$, where $c \sim 0.3$. Here again, these mesoscopic fluctuations scale as $1/\sqrt{g}$ and are extremely small compared to the peak width at weak disorder. In the relevant conductance range for our system $g \in [20 - 100]$, we obtain $\sigma_{E_{\max}} \in [0.5, 1.1]\%$, in excellent agreement with the 1% obtained experimentally [see Fig. 2(d)]. We compare these results for a weakly disordered phase with what was obtained in much more disordered niobium nitride (NbN) thin films ($g \sim 2$) where the relative gap fluctuations are of the order of 6% [43], in good agreement with the theory (7%) and much higher than what we measure here.

D. LDOS variance: Comparison with experiments

We now attempt to quantitatively compare our theoretical analysis for the energy-dependent LDOS fluctuations with our experiments on the SIC phase of lead on silicon. Using Eq. (4), we compute the normalized variance of the tunneling conductance: $\sigma_\eta^2 = \langle \delta\eta(V)^2\rangle_r/\langle\eta(V)\rangle_r^2$ at a bias voltage V. Here, we take into account the tip density of states and variations of the tip height above the sample during the measurement. All details are given in Appendix B. The formula we obtain for σ_η^2 [Eq. (B5)] is a straightforward energy integration of the density of states correlator given in Eq. (4).

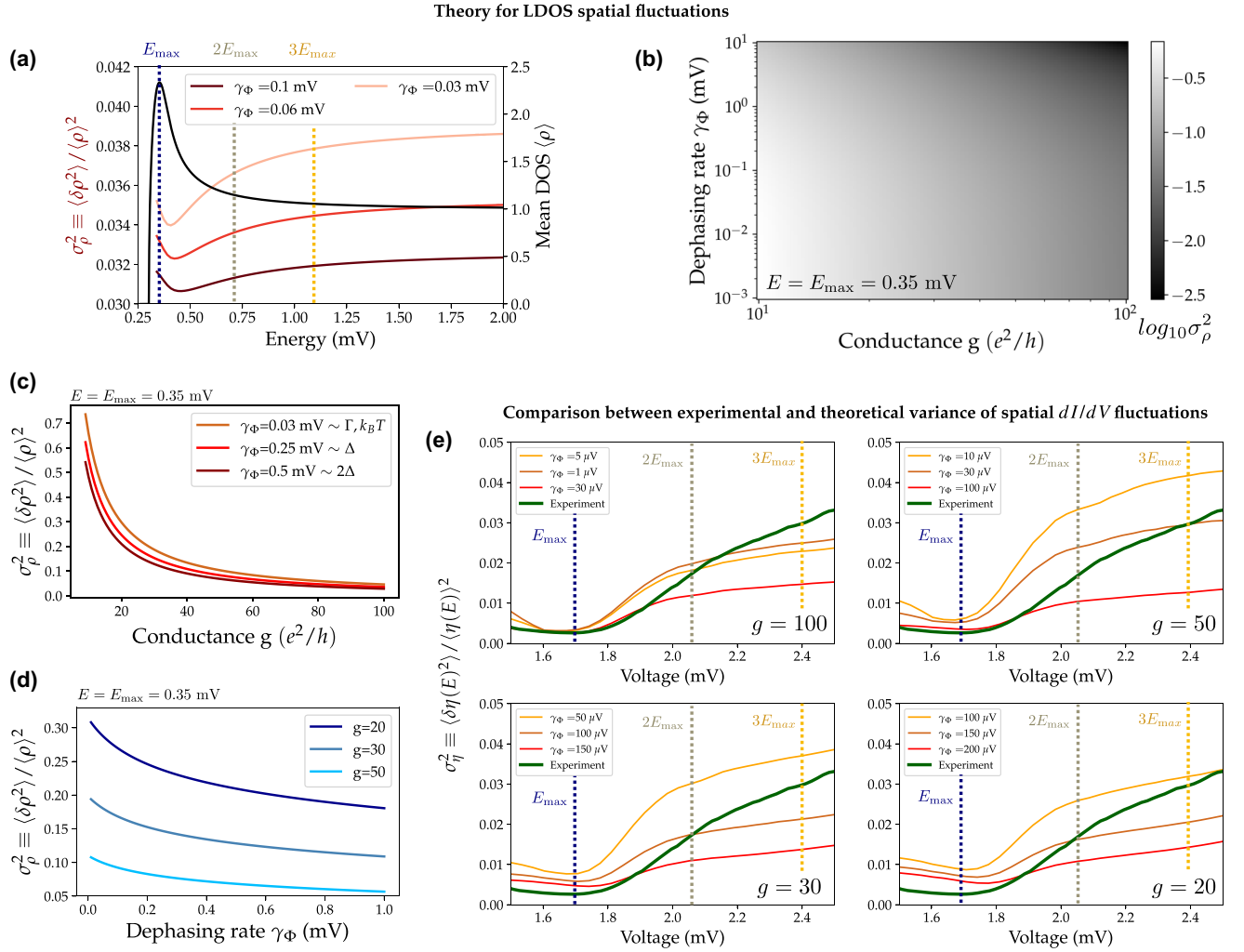

FIG. 3. Analysis of tunneling conductance fluctuations. In (a)–(d), we describe the fluctuations of the density of states computed semianalytically as a function of energy E, conductance g, and effective dephasing rate γ_Φ. In (a), we show the energy dependence of the normalized variance σ_ρ^2 (red) at $g = 30$ and several values of $\gamma_\Phi \in \{0.03, 0.06, 0.1\}$mV. In black, we show the mean density of states used for the calculation (solution of the Usadel equation; see Appendix A). In (b)–(d), we now fix the energy at $E_{\max} = 0.35$ mV and plot in (b) a color map of the log of σ_ρ^2 as a function of both conductance and dephasing rate. In (c), we show the dependence of σ_ρ^2 on conductance for $\gamma_\Phi \in \{0.03, 0.25, 0.5\}$ mV. In (d), we show the dependence on the dephasing rate for g $\in \{20, 30, 50\}$. In (e), we compare the experimentally measured normalized variance of tunneling conductance σ_η^2 with the one computed semianalytically from the density of states correlations [Eq. (B5), derived in Appendix B from Eq.(4)]. We plot the theoretical prediction for $g \in \{20, 30, 50, 100\}$ and the levels of dephasing which best reproduce the experimental data in each case. We stress that no free parameter is used here.

The tunneling conductance variance can then be compared to the experimentally measured σ^2_{exp} (in green) in Fig. 3(e). The thin lines are semianalytical calculations of σ_η for $g \in \{20, 30, 50, 100\}$ from Eq. (B5). For each value of g, we plot the theoretical curve for a few dephasing rates γ_Φ which best reproduce the experimental variance. We stress that no free parameter is used here because g takes very reasonable values for the SIC phase [35,38], while the dephasing rate γ_Φ is constrained in a rather narrow window of physically relevant energies, $\gamma_\Phi \in [1, 150]$ μeV $\sim [k_B T/30, \Delta_{\text{SIC}}/2]$. We obtain excellent quantitative agreement between experiment and theoretical predictions for a range of parameters corresponding to $g \in [50, 100]$, where the energy dependence of the normalized variance close to the coherence peak is very nicely reproduced.

Thus, we claim that emergent dI/dV spatial fluctuations in the 2D superconductor are a direct probe of coherent diffusion, well reproduced by a simple analytical model (Sec. III A). Although a quantitative extraction of γ_Φ is difficult in our case, our results show that scanning tunneling spectroscopy intrinsically allows for a local measurement of both dimensionless conductance and electronic coherence length. This noninvasive local probe explores structurally optimized regions far from step edges or contacts. This direct probe of electronic diffusion should be considered complementary to transport measurements. Moreover, it shows a huge, yet almost unexplored, potential for improvement through the detailed analysis of spatial correlations and, in particular, of the spatial structure of wave functions, which is expected to be the very cause of multifractal T_c enhance-

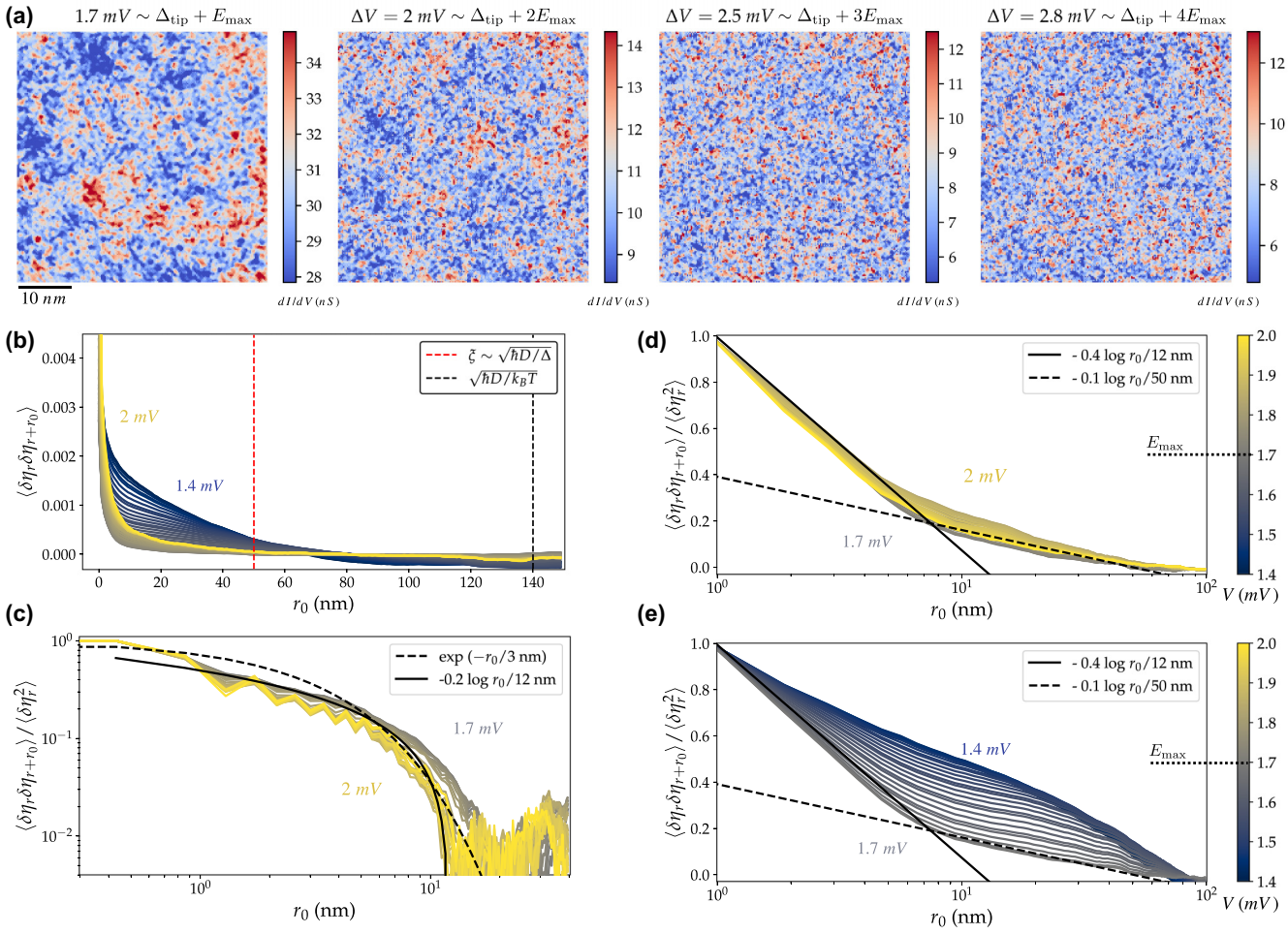

FIG. 4. dI/dV spatial correlations. In (a), we show several isoenergy high-resolution differential conductance maps for $E = V - \Delta_{\text{tip}} \in \{1, 2, 3, 4\}E_{\text{max}}$. In (b), we show the angle-averaged two-point correlations on large-scale maps as a function of distance and bias voltage [color scale for (b)–(e) is given in (d) and (e)]. In this plot, we also show the position of superconducting coherence length ξ (red) and the diffusion length corresponding to the energy scale $k_B T \sim 30$ μeV (black). In (c), we plot the angle-averaged autocorrelation computed on small-scale maps. In (d) and (e), we use lin-log scales to evidence the peculiar behavior of the autocorrelation (normalized by its zero-distance value). In (d), we focus on energies below E_{max}, and in (e), we focus on energies above E_{max}.

ment. In this regard, creating constant-height spectroscopic maps would allow a more direct comparison to theoretical predictions and is therefore a very exciting perspective.

IV. SPATIAL CORRELATIONS

After considering the variance of the isoenergy maps and thus disregarding the spatial structure of dI/dV fluctuations, we briefly focus on the analysis of the spatial correlations of the local conductance $\langle \delta\eta_r \delta\eta_{r+r_0} \rangle_r$. In Fig. 4(a), we show several high-resolution conductance maps at various energies above the coherence peak $E = V - \Delta_{\text{tip}} \in \{0.35, 0.7, 1.2, 1.5\}$ mV $\sim \{1, 2, 3, 4\}E_{\text{max}}$. We observe very clearly that large-scale spatial structures at E_{max} tend to disappear with increasing energy.

To explore the isoenergy spatial correlations of tunneling conductance, we plot in Fig. 4(b) the angle-averaged two-point correlation function as a function of distance r_0. The color of the curve represents the energy at which it is measured. In Fig. 4(c), we give a log-log representation of the autocorrelation function for high-resolution maps (normalized by its value at 0.1 nm). To better show the angle-averaged radial decay at various energies on large-scale 250 nm maps, we normalize the autocorrelation by its value at $r_0 = 1$ nm and plot it for energies below E_{max} in Fig. 4(d) and above E_{max} in Fig. 4(e), where a curve's color indicates its energy between 1.4 and 2 mV. It is apparent that above E_{max}, these autocorrelation profiles depend only very weakly on energy. In Fig. 4(d), we show that the spatial autocorrelation function has a short-range regime with steep decay up to approximately 10 nm followed by a long-range regime with a slower decay. As made visible by the black lines, two apparently log-decay regimes are identified with characteristic distance slopes of 12 and 50 nm for the short- and long-range regimes, respectively. Although they are not true correlation lengths, these two characteristic lengths in the autocorrelation function seem very natural because a value of 10 nm corresponds to the typical nanocrystal size of the SIC monolayer and a value of 50 nm corresponds to its superconducting coherence length.

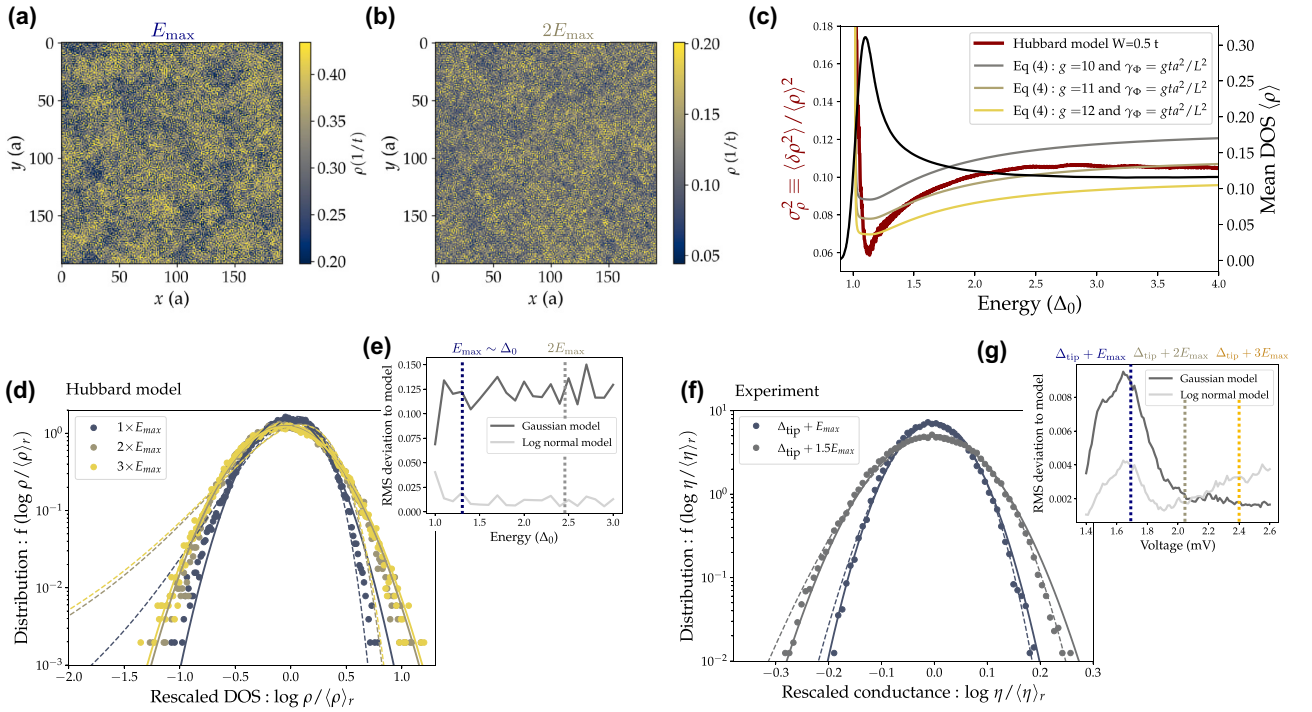

FIG. 5. Disordered attractive Hubbard model and LDOS distributions. In (a) and (b), we show the local density of states maps taken at $E = E_{\max}$ and $2E_{\max}$ using the attractive Hubbard model. The density of states is given in units of $1/t$, with t being the hopping energy. In (c), we show the mean density of states of the numerical model (black line) along with the normalized variance σ^2 (red). We plot the analytical prediction from Eq. (4) for $g \in \{10, 11, 12\}$. We stress that no free parameter has been optimized. In (d), we plot the LDOS distribution at fixed energy along with the corresponding Gaussian (dotted line) and log-normal (solid line) distributions (i.e., same variance). Distribution functions are given in Appendix C. In (e), we show the rms deviation from, respectively, Gaussian (dark gray) and log normal (light gray) models. Panels (f) and (g) are analogous to (d) and (e) for the experimental dI/dV distribution.

To deepen our understanding of these LDOS fluctuations, we complement our experimental work with a numerical study of superconducting electrons on a 2D disordered lattice in the weak-disorder regime. The great similarity between experimental models and our fully self-consistent tight-binding model then allows us to make a very precise comparison between numerical, experimental, and analytical studies.

V. NUMERICAL STUDY OF LDOS FLUCTUATIONS WITH THE ATTRACTIVE HUBBARD MODEL

We write and solve a tight-binding model tailored to match the experimental system: a weakly disordered 2D diffusive superconductor of comparable conductivity and dephasing rates. We consider the attractive-U Hubbard model on the square lattice in two dimensions with double-periodic boundary conditions. Within the mean-field approximation the Hamiltonian reads ($U > 0$)

$$\hat{H} = -t \sum_{\langle i,j\rangle,\sigma} \hat{c}^\dagger_{i,\sigma} \hat{c}_{j,\sigma} + \sum_{i,\sigma} [V_i - \mu - Un(\boldsymbol{r}_i)/2] \hat{n}_{i,\sigma} + \sum_i \Delta(\boldsymbol{r}_i) \hat{c}_{i,\uparrow} \hat{c}_{i,\downarrow} + \text{H.c.}, \tag{5}$$

where $\hat{c}^\dagger_{j,\sigma}$ and $\hat{c}_{j,\sigma}$ denote the creation and annihilation operators of an electron with spin $\sigma = \pm 1/2$ on site j. The on-site disorder potential is drawn from a box distribution, $V_i \in [-W, W]$, with the disorder strength fixed at $W = 0.5$ in an attempt to match the experimental disorder strength. The chemical potential μ fixes the filling factor to 0.3. Throughout this work the interaction is taken to be $U = 2.2t$, and the system size is $L = 192$; the local occupation number $n(\mathbf{r}_i)$ and the pairing amplitude $\Delta(\mathbf{r}_i)$ are determined self-consistently:

$$n(\mathbf{r}_i) = \sum_\sigma \langle \hat{n}_{i,\sigma} \rangle, \quad \Delta(\mathbf{r}_i) = U \langle \hat{c}^\dagger_{i,\downarrow} \hat{c}^\dagger_{i,\uparrow} \rangle, \tag{6}$$

where $\hat{n}_{i,\sigma} = \hat{c}^\dagger_{i,\sigma} \hat{c}_{i,\sigma}$. We solve Eqs. (5) and (6) iteratively until a self-consistent solution is obtained (see Ref. [19] for further computational details). The ensemble averaging typically involves more than 100 samples, and the density of states is computed by averaging on an energy scale of $\langle\Delta\rangle/10$, in good agreement with the experimental situation ($\Gamma_{\text{tip}} = 20$ μeV $\sim \Delta_{\text{SIC}}/10$). We note that the numerical model does not reproduce the strong spin-orbit coupling of the SIC phase. Nevertheless, as explained in Sec. III A, the theoretical analysis predicts that strong spin-orbit coupling reduces the normalized standard deviation σ by a factor of 2 [23]. Keeping this twofold reduction in mind allows us to quantitatively compare experiments, analytical predictions, and numerical calculations.

In Fig. 5, we show the results of the numerical investigation and compare them with both the analytical theory derived earlier and the experimental results. We check that, as expected at weak disorder [23] and in quantitative agreement with the experiment, the spectral gap shows very small

fluctuations of about 2%. In Figs. 5(a) and 5(b), we show local density of states maps at $E = E_{\max}$ and $E = 2E_{\max}$. In excellent agreement with the experimental results (Fig. 4), we observe that LDOS fluctuations exhibit much longer range correlations close to $E_{\max}$ than at higher energy [see the size of the structures in Figs. 5(a) and 5(b)].

A. Gap width fluctuations

Following the analysis in Sec. III C for the analytical theory, we start our systematic comparison between the SIC phase and the attractive Hubbard model using gap fluctuations. In the self-consistent numerical model, we find relative fluctuations $\sigma_{E_{\max}} \sim 2\%$ slightly above our experimental result of 1% [see Fig. 2(c)]. A detailed study of the spectral gap and order parameter statistics in the disordered attractive Hubbard model is underway [44].

B. Normalized variance

Like in the experimental section above, we now proceed to study the normalized variance of the LDOS spatial fluctuations. In Fig. 5(c), we show the mean density of states of the numerical model (black line) along with the normalized variance σ^2 (red). We compare the numerically obtained LDOS variance with the analytical prediction derived from Eq. (4) depending on the dimensionless conductance g and dephasing rate γ_Φ. As our tight–binding approach considers solutions of the stationary Schrödinger equation, it does not include dephasing. γ_Φ is thus substituted by a Thouless energy corresponding to diffusive motion at the scale of the system size: $\gamma_\Phi = \frac{\hbar D}{L^2}$. Knowing the density of states and Fermi velocity of the 2D electron gas, we manage to compute Eq. (4) as a function of a single parameter, the dimensionless conductance g (with $\gamma_\Phi = gta^2/L^2$). We find that $g \sim 10$ almost perfectly reproduces the numerical results (red) in the entire energy range we considered. This lower conductance compared to the SIC phase is fully consistent with the gap width fluctuations: two times higher for the model than for experiments. We conclude, based on enhanced fluctuations of both the LDOS and the gap width, along with a similar energy dependences, that the tight-binding system is slightly more disordered than its experimental counterpart.

C. LDOS distributions

We already know from several experiments that disordered systems tend to yield log-normal LDOS distributions [7,8]. More precisely, close to the Anderson transition, a log-normal distribution of the LDOS is expected [4,16,21]. In the low-disorder regime relevant here, log-normal distributions for the LDOS have also been predicted analytically [45] and observed in numerical models [22].

Here, we study the distribution functions of both our experimental dI/dV maps and the ones obtained from the attractive Hubbard model. Starting with the numerical results, we plot in Fig. 5(d) the distribution of the LDOS distribution at fixed energy along with the corresponding (i.e., same variance) Gaussian and log-normal laws (see Appendix C). A clear log-normal behavior is identified in the entire energy range between $E_{\max}$ and $3E_{\max}$, as confirmed by Fig. 5(e), which compares the rms deviation of the distribution to the Gaussian log-normal models. Turning to the experimental data, we show in Fig. 5(f) the dI/dV distribution with Gaussian (dotted line) and log-normal (solid line) laws with the same variance at voltages corresponding to $E_{\max}$ and $1.5E_{\max}$. Like before, we plot in Fig. 5(g) the rms deviation of the Gaussian and log-normal models. The fact that the log-normal model is more accurate hints at the multifractal nature of the LDOS fluctuations close to the superconducting coherence peak.

VI. CONCLUSION

As a model system for a two-dimensional weakly disordered superconductor for which multifractal superconductivity is being actively pursued, we prepared a single layer of lead on Si(111), where electrons are antilocalized in a controlled crystalline disorder and become superconducting below 1.8 K. Using scanning tunneling spectroscopy, we reported the measurement of tunneling conductance fluctuations with high spatial and spectral resolutions on scales exceeding the superconducting coherence length. To support our analysis, we used two theoretical approaches, a semianalytical one and a numerical one. Our numerical approach consisted of an attractive Hubbard model with the disorder level tuned to match the experiment and probed both gap width and LDOS fluctuations close to the superconducting coherence peak. Our experimental, semianalytical, and numerical results were shown to be quantitatively consistent with the mesoscopic fluctuation physics in the weakly antilocalized regime usually probed with transport measurements. The LDOS fluctuation's amplitude depends on two local parameters which can be probed and quantitatively extracted in this way: the metal's conductance and the effective electronic dephasing rate.

ACKNOWLEDGMENTS

This work was supported by the French national research fund managed by the ANR through the project RODESIS under Contract No. ANR-16-CE30-0011-01. The work of I.B. was funded in part by the Russian Ministry of Science and Higher Education and the Basic Research Program of HSE, and the Russian Foundation for Basic Research, Grant No. 20-52-12013.

APPENDIX A: MEAN DENSITY OF STATES

We use the Usadel model [37,46] to describe the diffusive SIC phase because the mean free path is much smaller than the superconducting coherence length in this sample: $\ell \sim 1$ nm $\ll \xi \sim 50$ nm. In more detail, we use the spectral angle θ_E parametrization, with θ_E being a solution of a homogeneous Usadel equation with the depairing term Γ:

$$iE\sin(\theta_E) + \Delta\cos(\theta_E) - \Gamma\sin(\theta_E)\cos(\theta_E) = 0. \quad \text{(A1)}$$

The solution of this equation θ_E yields $X_E = \cos(\theta_E)$ ($= \frac{E}{\sqrt{E^2-\Delta^2}}$ at $\Gamma = 0$), from which the density of states $\mathrm{Re}(X_E)$ is obtained.

Using Eqs. (A2) and (A1), we convolve the density of states of the tip with that of the sample (along with the Fermi distribution at 300 mK) in order to reproduce the mean differ-

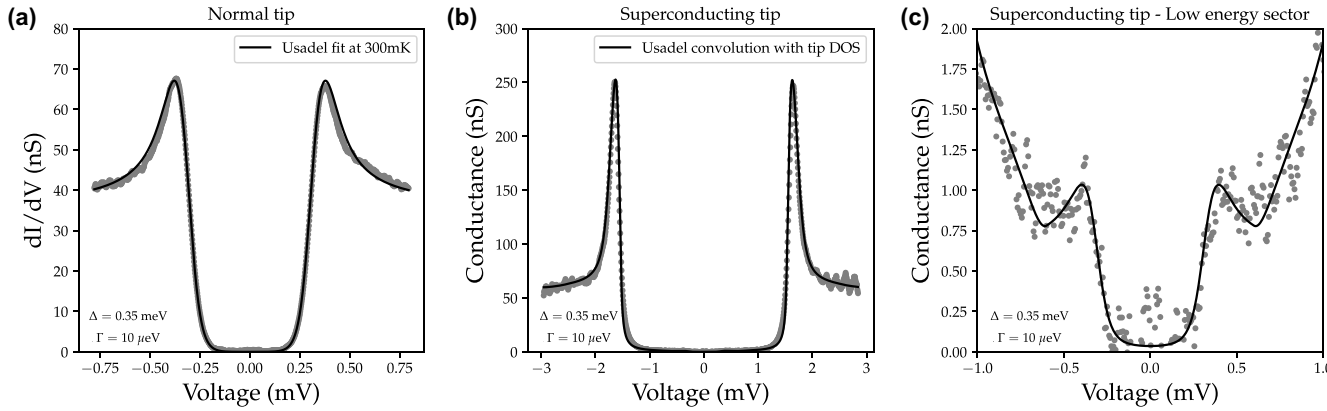

FIG. 6. Fit of the mean conductance. In (a), the mean differential conductance measured with a platinum tip is shown as a function of the bias voltage along with the best Usadel fit. In (b), we show the mean dI/dV curve of the large-scale spectroscopic map measured with a bulk lead tip, while the solid line is a convolution of the Usadel density of states for the sample with the tip density of states at 300 mK. In (c), we show a zoom of the low-energy sector for the superconducting tip allowing a very precise extraction of Δ_{SIC} and Γ_{SIC} (see the excellent agreement of the Usadel model with the experiment).

ential conductance:

$$I \propto \int \rho_{\mathrm{tip}}(E - eV)\rho_{\mathrm{SIC}}(E, \boldsymbol{r})[f(E) - f(E - eV)]dE, \tag{A2}$$

where ρ_{tip} and ρ_{SIC} are, respectively, the energy-dependent DOSs of the tip and the SIC phase. As detailed in Fig. 6, we find that the lead tip is very well described by a Usadel superconductor ($\Delta_{\mathrm{tip}} = 1.345$ meV, $\Gamma_{\mathrm{tip}} = 20$ μeV). The SIC phase is found to be very well described by $\Delta_{\mathrm{SIC}} = 0.35$ meV and $\Gamma_{\mathrm{SIC}} = 10$ μeV, in excellent agreement with additional measurements using a normal tip [Figs. 1(b) and 6(a)] and with earlier works [35,38].

APPENDIX B: DIFFERENTIAL CONDUCTANCE VARIANCE COMPUTATION

We now attempt to rationalize the tunneling conductance spatial fluctuations. Considering a simplified expression for the tunneling current, we write it as a zero-temperature convolution of the tip and sample density of states (A2). Experimentally, the tip's height above the sample and thus the transmission's coefficient t are not constant but are rather controlled by fixing the high voltage current $I(V_\Lambda = 3\ \mathrm{mV})$ to 20 pA. Trying to estimate density of states leads us to compute

$$\eta(V, \boldsymbol{r}) = \frac{\overline{I(V_\Lambda)}}{I(V_\Lambda, \boldsymbol{r})}\frac{\partial I}{\partial V}(V, \boldsymbol{r}). \tag{B1}$$

At $T = 0$, we write, for the tunneling current I and the tunneling conductance dI/dV,

$$I = |t|^2 \int_0^V dE\, \rho_{\mathrm{tip}}(E - eV)\rho(E, \boldsymbol{r}), \qquad \frac{\partial I}{\partial V} = |t|^2 \rho_{\mathrm{tip}}(0)\rho(V, \boldsymbol{r}) - |t|^2 \int_0^V dE\, \rho'_{\mathrm{tip}}(E - V)\rho(E, \boldsymbol{r}), \tag{B2}$$

where $\rho'_{\mathrm{tip}}(E) \equiv d\rho_{\mathrm{tip}}(E)/dE$. It is convenient to introduce the following notations:

$$\bar{j}(V) = \int_0^V dE\, \rho_{\mathrm{tip}}(E - V)\bar{\rho}(E), \qquad \bar{j}'(V) = \rho_{\mathrm{tip}}(0)\bar{\rho}(V) - \int_0^V dE\, \rho'_{\mathrm{tip}}(E - V)\bar{\rho}(E). \tag{B3}$$

Assuming that fluctuations $\delta\rho(E, \boldsymbol{r}) = \rho(E, \boldsymbol{r}) - \bar{\rho}(E)$ near the average DOS $\bar{\rho}(E)$ are weak, we find

$$\frac{\delta\eta(V, \boldsymbol{r})}{\overline{I(V_\Lambda)}} = \frac{\rho_{\mathrm{tip}}(0)\delta\rho(V, \boldsymbol{r})}{\bar{j}(V_\Lambda)} - \int_0^\infty dE\, \delta\rho(E, \boldsymbol{r})\frac{\rho'_{\mathrm{tip}}(E - V)\bar{j}(V_\Lambda)\Theta(V - E) + \rho_{\mathrm{tip}}(E - V_\Lambda)\bar{j}'(V)\Theta(V_\Lambda - E)}{[\bar{j}(V_\Lambda)]^2}. \tag{B4}$$

Here, $\Theta(x) = 1$ for $x > 0$ and zero otherwise. Hence, we obtain

$$\begin{aligned}\frac{\langle\delta\eta(V_1, \boldsymbol{r}_1)\delta\eta(V_2, \boldsymbol{r}_2)\rangle}{[\overline{I(V_\Lambda)}]^2} = {} & \frac{\rho^2_{\mathrm{tip}}(0)}{\bar{j}(V_\Lambda)\bar{j}(V_\Lambda)}\langle\delta\rho(V_1, \boldsymbol{r}_1)\delta\rho(V_2, \boldsymbol{r}_2)\rangle - \frac{\rho_{\mathrm{tip}}(0)}{\bar{j}(V_\Lambda)}\int_0^\infty dE\, \langle\delta\rho(V_1, \boldsymbol{r}_1)\delta\rho(E, \boldsymbol{r}_2)\rangle \\ & \times \frac{\rho'_{\mathrm{tip}}(E - V_2)\bar{j}(V_\Lambda)\Theta(V_2 - E) + \rho_{\mathrm{tip}}(E - V_\Lambda)\bar{j}'(V_2)\Theta(V_\Lambda - E)}{[\bar{j}(V_\Lambda)]^2} - \frac{\rho_{\mathrm{tip}}(0)}{\bar{j}(V_\Lambda)} \\ & \times \int_0^\infty dE\, \langle\delta\rho(V_2, \boldsymbol{r}_2)\delta\rho(E, \boldsymbol{r}_1)\rangle\frac{\rho'_{\mathrm{tip}}(E - V_1)\bar{j}(V_\Lambda)\Theta(V_1 - E) + \rho_{\mathrm{tip}}(E - V_\Lambda)\bar{j}'(V_1)\Theta(V_\Lambda - E)}{[\bar{j}(V_\Lambda)]^2}\end{aligned}$$

$$+\int_0^\infty dE_1\int_0^\infty dE_2\,\langle\delta\rho(E_1,\boldsymbol{r}_1)\delta\rho(E_2,\boldsymbol{r}_2)\rangle$$
$$\times\frac{\rho'_{\rm tip}(E_1-V_1)\bar{j}(V_\Lambda)\Theta(V_1-E_1)+\rho_{\rm tip}(E_1-V_\Lambda)\bar{j}'(V_1)\Theta(V_\Lambda-E_1)}{[\bar{j}(V_\Lambda)]^2}$$
$$\times\frac{\rho'_{\rm tip}(E_2-V_2)\bar{j}(V_\Lambda)\Theta(V_2-E_2)+\rho_{\rm tip}(E_2-V_\Lambda)\bar{j}'(V_2)\Theta(V_\Lambda-E_2)}{[\bar{j}(V_\Lambda)]^2}. \tag{B5}$$

APPENDIX C: ISOENERGY LDOS DISTRIBUTION

We compare the isoenergy dI/dV distributions to Gaussian and log-normal models of variance σ. The distribution of the logarithm of the normalized density of states $x=\ln[\rho(E,r)/\langle\rho(E,r)\rangle_r]$ for a Gaussian distribution is written as

$$f_{\text{log-n}}(x)=\frac{1}{\sqrt{2\pi\sigma^2}}\exp\left[x-\frac{(e^x-1)^2}{2\sigma^2}\right]. \tag{C1}$$

For a log-normal distribution, which is expected in the theoretical analysis and recovered in the numerical work, the log of the normalized LDOS x is distributed as follows:

$$f_{\rm n}(x)=\frac{1}{\sqrt{2\pi\sigma^2}}\exp\left[\frac{-(x+\sigma^2/2)^2}{2\sigma^2}\right]. \tag{C2}$$

APPENDIX D: GAP WIDTH FLUCTUATIONS

Let us assume that the LDOS $\rho(E)$ at a given realization of disorder potential has the single maximum (for positive energies) at $E_{\rm max}$ as a function of energy. Assuming the deviation $\delta E_{\rm max}=E_{\rm max}-\overline{E}_{\rm max}$ from the energy $\overline{E}_{\rm max}$ of the maximum in the average LDOS $\overline{\rho}(E)$, we can write

$$0=\rho'(E_{\rm max})\simeq\bar{\rho}'(E_{\rm max})+\delta\rho'(E_{\rm max})\simeq\bar{\rho}'(\bar{E}_{\rm max})+\bar{\rho}''(\bar{E}_{\rm max})\delta E_{\rm max}+\delta\rho'(E_{\rm max})\simeq\bar{\rho}''(\bar{E}_{\rm max})\delta E_{\rm max}+\delta\rho'(E_{\rm max})$$
$$\Longrightarrow\quad\overline{(\delta E_{\rm max})^2}\simeq\frac{\overline{[\delta\rho'(\bar{E}_{\rm max})]^2}}{[\bar{\rho}''(\bar{E}_{\rm max})]^2}. \tag{D1}$$

Here, we can the variance of the energy derivative of the LDOS read from Eq. (4).

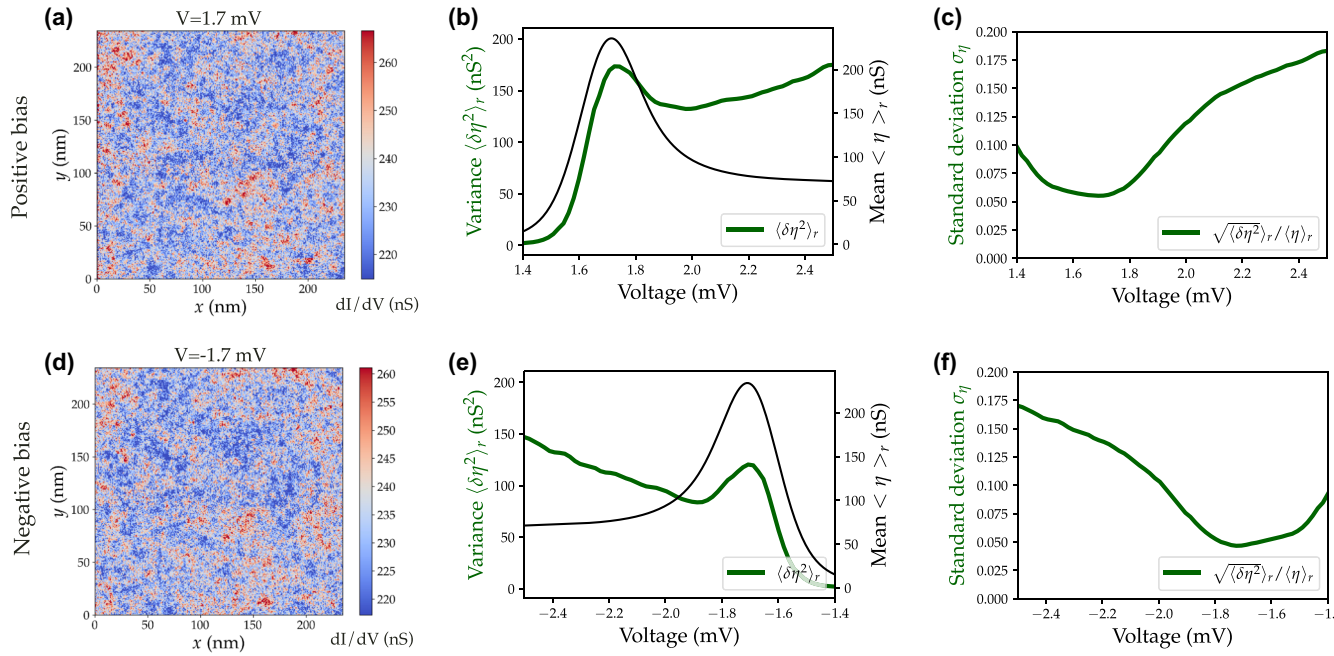

FIG. 7. Symmetry with respect to Fermi energy. For positive bias voltage, we show (a) the LDOS map at $E_{\rm max}=1.7$ mV, (b) the variance and mean value of tunneling conductance, and (c) the normalized standard deviation σ_η. In (d)–(f), we show the corresponding data for negative bias voltage.

The quantity X_E for the Usadel equation (A1) near $E_{\max}$ can be approximated as (assuming $\Gamma \ll \Delta$) [47,48]

$$X_E = \left(\frac{\Delta}{\Gamma}\right)^{1/3} f\left(\frac{E - E_g}{\Gamma^{2/3}\Delta^{1/3}}\right), \tag{D2}$$

where the spectral gap $E_g = \Delta[1 - 3(\Gamma/\Delta)^{2/3}/2]$. Then we find the following estimates:

$$\overline{[\delta\rho'(\bar{E}_{\max})]^2} \simeq \frac{c_1}{4\pi g}\frac{\Delta^2}{\Gamma^2}, \quad \bar{\rho}''(\bar{E}_{\max}) \simeq c_2\left(\frac{\Delta}{\Gamma}\right)^{5/3}, \quad \overline{(\delta E_{\max})^2} \simeq \frac{c}{g}\left(\frac{\Gamma}{\Delta}\right)^{4/3}, \tag{D3}$$

where $c_1 \approx 0.23$, $c_2 \approx -0.24$, and $c = c_1/(4\pi c_2^2) \approx 0.32$.

APPENDIX E: SYMMETRY WITH RESPECT TO THE FERMI ENERGY

Our analytical calculations predict the same normalized variance in the negative and positive energy ranges. It is important for the consistency of our analysis to check this symmetry in the experiments. In Fig. 7, we show that not only the visual aspect of the LDOS map at the coherence peak but also the energy-dependent normalized LDOS standard deviation is perfectly symmetric with respect to the Fermi level.

[1] E. Akkermans and G. Montambaux, *Mesoscopic Physics of Electrons and Photons* (Cambridge University Press, Cambridge, 2007).
[2] F. Wegner, Z. Phys. B **36**, 209 (1980).
[3] C. Castellani and L. Pelitit, J. Phys. A **19**, L429 (1986).
[4] I. V. Lerner, Phys. Lett. A **133**, 253 (1988).
[5] R. Carminati, A. Cazé, D. Cao, F. Peragut, V. Krachmalnicoff, R. Pierrat, and Y. De Wilde, Surf. Sci. Rep. **70**, 1 (2015).
[6] V. Krachmalnicoff, E. Castanié, Y. De Wilde, and R. Carminati, Phys. Rev. Lett. **105**, 183901 (2010).
[7] A. Richardella, P. Roushan, S. Mack, B. Zhou, D. A. Huse, D. D. Awschalom, and A. Yazdani, Science **327**, 665 (2010).
[8] B. Jäck, F. Zinser, E. J. König, S. N. P. Wissing, A. B. Schmidt, M. Donath, K. Kern, and C. R. Ast, Phys. Rev. Res. **3**, 013022 (2021).
[9] K. Zhao, H. Lin, X. Xiao, W. Huang, W. Yao, M. Yan, Y. Xing, Q. Zhang, Z.-X. Li, S. Hoshino, J. Wang, S. Zhou, L. Gu, M. S. Bahramy, H. Yao, N. Nagaosa, Q.-K. Xue, K. T. Law, X. Chen, and S.-H. Ji, Nat. Phys. **15**, 904 (2019).
[10] M. Morgenstern, J. Klijn, C. Meyer, and R. Wiesendanger, Phys. Rev. Lett. **90**, 056804 (2003).
[11] V. F. Gantmakher and V. T. Dolgopolov, Phys.-Usp. **53**, 1 (2010).
[12] B. Sacépé, M. Feigel'man, and T. M. Klapwijk, Nat. Phys. **16**, 734 (2020).
[13] M. Feigel'man, L. Ioffe, V. Kravtsov, and E. Cuevas, Ann. Phys. (NY) **325**, 1390 (2010).
[14] L. Dell'Anna, Phys. Rev. B **88**, 195139 (2013).
[15] I. S. Burmistrov, I. V. Gornyi, and A. D. Mirlin, Phys. Rev. B **92**, 014506 (2015).
[16] I. S. Burmistrov, I. V. Gornyi, and A. D. Mirlin, Phys. Rev. B **93**, 205432 (2016).
[17] M. N. Gastiasoro and B. M. Andersen, Phys. Rev. B **98**, 184510 (2018).
[18] B. Fan and A. M. García-García, Phys. Rev. B **101**, 104509 (2020).
[19] M. Stosiek, B. Lang, and F. Evers, Phys. Rev. B **101**, 144503 (2020).
[20] B. Fan and A. M. García-García, Phys. Rev. B **102**, 184507 (2020).
[21] I. S. Burmistrov, I. V. Gornyi, and A. D. Mirlin, Ann. Phys. **435**, 168499 (2021).
[22] M. Stosiek, F. Evers, and I. S. Burmistrov, Phys. Rev. Res. **3**, L042016 (2021).
[23] E. S. Andriyakhina and I. S. Burmistrov, J. Exp. Theor. Phys. **135**, 484 (2022).
[24] X. Zhang and M. S. Foster, Phys. Rev. B **106**, L180503 (2022).
[25] M. V. Feigel'man, L. B. Ioffe, V. E. Kravtsov, and E. A. Yuzbashyan, Phys. Rev. Lett. **98**, 027001 (2007).
[26] I. S. Burmistrov, I. V. Gornyi, and A. D. Mirlin, Phys. Rev. Lett. **108**, 017002 (2012).
[27] C. Rubio-Verdu, A. M. Garcia-Garcia, H. Ryu, D.-J. Choi, J. Zaldivar, S. Tang, B. Fan, Z.-X. Shen, S.-K. Mo, J. I. Pascual, and M. M. Ugeda, Nano Lett. **20**, 5111 (2020).
[28] D. Wander, Investigation of mesoscopic superconductivity and quantum hall effect by low temperature scanning tunneling microscopy, Theses, Université Grenoble Alpes, 2022.
[29] B. Sacepe, C. Chapelier, T. I. Baturina, V. M. Vinokur, M. R. Baklanov, and M. Sanquer, Phys. Rev. Lett. **101**, 157006 (2008).
[30] M. Mondal, A. Kamlapure, M. Chand, G. Saraswat, S. Kumar, J. Jesudasan, L. Benfatto, V. Tripathi, and P. Raychaudhuri, Phys. Rev. Lett. **106**, 047001 (2011).
[31] Y. Noat, V. Cherkez, C. Brun, T. Cren, C. Carbillet, F. Debontridder, K. Ilin, M. Siegel, A. Semenov, H.-W. Hübers, and D. Roditchev, Phys. Rev. B **88**, 014503 (2013).
[32] D. Sherman, B. Gorshunov, S. Poran, N. Trivedi, E. Farber, M. Dressel, and A. Frydman, Phys. Rev. B **89**, 035149 (2014).
[33] B. Sacépé, C. Chapelier, T. I. Baturina, V. M. Vinokur, M. R. Baklanov, and M. Sanquer, Nat. Commun. **1**, 140 (2010).
[34] B. Sacépé, T. Dubouchet, C. Chapelier, M. Sanquer, M. Ovadia, D. Shahar, M. Feigel'man, and L. Ioffe, Nat. Phys. **7**, 239 (2011).
[35] V. Cherkez, J. C. Cuevas, C. Brun, T. Cren, G. Ménard, F. Debontridder, V. S. Stolyarov, and D. Roditchev, Phys. Rev. X **4**, 011033 (2014).

[36] C. Brun, T. Cren, and D. Roditchev, Supercond. Sci. Technol. **30**, 013003 (2017).
[37] K. D. Usadel, Phys. Rev. Lett. **25**, 507 (1970).
[38] C. Brun, T. Cren, V. Cherkez, F. Debontridder, S. Pons, D. Fokin, M. C. Tringides, S. Bozhko, L. B. Ioffe, B. L. Altshuler, and D. Roditchev, Nat. Phys. **10**, 444 (2014).
[39] A. Ghosal, M. Randeria, and N. Trivedi, Phys. Rev. B **65**, 014501 (2001).
[40] P. A. Lee and T. V. Ramakrishnan, Rev. Mod. Phys. **57**, 287 (1985).
[41] B. L. Altshuler and A. G. Aronov, *Modern Problems in Condensed Matter Sciences*, edited by A. L. Efros and M. Pollak, Electron–Electron Interactions in Disordered Systems Vol. 10 (Elsevier, North-Holland, 1985), pp. 1–153.
[42] W. H. Choi, H. Koh, E. Rotenberg, and H. W. Yeom, Phys. Rev. B **75**, 075329 (2007).
[43] C. Carbillet, V. Cherkez, M. A. Skvortsov, M. V. Feigel'man, F. Debontridder, L. B. Ioffe, V. S. Stolyarov, K. Ilin, M. Siegel, D. Roditchev, T. Cren, and C. Brun, Phys. Rev. B **102**, 024504 (2020).
[44] J. Dieplinger, M. Stosiek, and F. Evers (unpublished).
[45] V. I. Fal'ko and K. B. Efetov, Europhys. Lett. **32**, 627 (1995).
[46] S. Gueron, Quasiparticles in a diffusive conductor: Interaction and paring, Theses, Université Pierre et Marie Curie - Paris VI, 1997.
[47] A. A. Abrikosov and L. P. Gor'kov, Z. Eksp. Teor. Fiz. **39**, 1781 (1960).
[48] Y. V. Fominov and M. A. Skvortsov, Phys. Rev. B **93**, 144511 (2016).